

# The Atomic and Electronic structure of 0° and 60° grain boundaries in MoS<sub>2</sub>

Terunobu Nakanishi<sup>⊥</sup>, Shoji Yoshida<sup>§</sup>, Kota Murase<sup>§</sup>, Osamu Takeuchi<sup>§</sup>, Takashi Taniguchi<sup>†</sup>, Kenji Watanabe<sup>†</sup>, Hidemi Shigekawa<sup>§</sup>, Hisanori Shinohara<sup>⊥,\*</sup>, and Ryo Kitaura<sup>⊥,\*</sup>

<sup>⊥</sup>Department of Chemistry, Nagoya University, Nagoya 464-8602, Japan

<sup>†</sup>Advanced Materials Laboratory, National Institute for Materials Science, 1-1 Namiki, Tsukuba 305-0044, Japan

<sup>§</sup>Faculty of Pure and Applied Sciences, University of Tsukuba, Tsukuba 305-8571, Japan

\*Corresponding Author: R. Kitaura and H. Shinohara

Tel: +81-52-789-2482, Fax: +81-52-747-6442,

E-mail: r.kitaura@nagoya-u.jp and noris@nagoya-u.jp

## ABSTRACT

We have investigated atomic and electronic structure of grain boundaries in monolayer MoS<sub>2</sub>, where relative angles between two different grains are 0 and 60 degree. The grain boundaries with specific relative angle have been formed with chemical vapor deposition growth on graphite and hexagonal boron nitride flakes; van der Waals interlayer interaction between MoS<sub>2</sub> and the flakes restricts the relative angle. Through scanning tunneling microscopy and spectroscopy measurements, we have found that the perfectly stitched structure between two different grains of MoS<sub>2</sub> was realized in the case of the 0 degree grain boundary. We also found that even with the perfectly stitched structure, valence band maximum and conduction band minimum shows significant blue shift, which probably arise from lattice strain at the boundary.

## 1. INTRODUCTION

A post-graphene material, transition metal dichalcogenide (TMD), has recently attracted a great deal of attention. TMDs have a long research history, but research on properties of monolayer TMDs, three-atom-thick atomic layers, has only recently been started.<sup>[1-3]</sup> One of the most distinct in TMDs from graphene is that TMDs can have sizable bandgap (~2 eV), leading to electronic and

optoelectronic applications of TMD atomic layers.<sup>[4]</sup> In fact, various TMD-based devices, including high-performance FET devices, light-emitting transistors, and photodetectors, have actually been demonstrated.<sup>[5-7]</sup> In conjunction with the flexibility arising from the ultrathin structure, flexible electronic and optoelectronic devices can also be made.<sup>[8,9]</sup> In addition, monolayer TMDs in 2H form can have valley-degree-of-freedom, which may lead to future novel electronic devices based on valleytronics.<sup>[10,11]</sup>

For future applications of TMDs for electronic and optoelectronic devices, wafer-scale monolayer TMDs grown by chemical vapor deposition (CVD) are indispensable.<sup>[12,13]</sup> Top-down approaches, such as mechanical exfoliation, are not compatible with wafer-scale monolayer TMDs, and a bottom-up approach is required for that purpose.<sup>[14]</sup> Crystal growth by CVD is a bottom-up approach to obtain thin films, having been successfully applied to grow various atomic layers, such as graphene, hexagonal boron nitrides (hBN), and TMDs.<sup>[15-20]</sup> In typical CVD growth of TMDs, solid sources such as metal oxides and elemental sulfur are used, and monolayer TMDs film with a lateral size of millimeters have been reported.<sup>[19,21]</sup> Recently, the growth of TMDs by metal-organic CVD (MOCVD) with volatile liquid sources has been successfully demonstrated, and MOCVD is a promising method to realize wafer-scale TMDs that are compatible with device applications.<sup>[22-24]</sup>

In CVD-grown large-area TMDs, grain boundaries (GBs) are inevitably formed, which can significantly alter the electronic and optical properties of TMDs.<sup>[25-28]</sup> During the CVD growth of TMDs, nuclei form at the beginning of the CVD process, growing to form a large-area continuous sheet of TMD with GBs. Because the orientation of nuclei is normally random, a wide variety of GB structures can be formed. For example, a GB with 7-5 and 8-4-4 membered rings forms in a CVD-grown MoS<sub>2</sub>, where midgap boundary states appear.<sup>[25,29-31]</sup> The existence of GB-induced midgap states significantly affects electronic transport across the boundary, leading to reduction of carrier mobility via additional carrier scattering at the GB.<sup>[25]</sup> Therefore, control of GB structure by controlling grain orientation and understanding the boundary-oriented electronic structure provide a basis for the realization of future TMD-based devices.

In this work, we have focused on orientation-limited growth of a TMD and investigation of localized boundary states using scanning tunneling microscopy (STM) and scanning tunneling spectroscopy (STS). The key for the successful control of crystal orientation in CVD growth of TMDs is the interaction between

TMDs and the substrates used in CVD processes. In conventional CVD growth of TMDs, SiO<sub>2</sub>/Si substrates with amorphous surfaces are used, leading to random crystal orientations of grown TMDs. In contrast, substrates with crystalline structures can limit the crystal orientation of grown TMDs through TMD-substrate interactions.<sup>[20,29,32,33]</sup> For the control of crystal orientation, we used hBN and graphite as substrates for CVD growth of TMDs. The atomically flat surfaces with three-fold (hBN) and six-fold rotation (graphite) symmetries successfully limited crystal orientations of grown TMD flakes; only two different orientations were observed. GBs between MoS<sub>2</sub> flakes with different orientations (relative angle of 60°) have 7-5 and 8-4-4 membered rings, where boundary states localized at 8-4-4 membered rings exist near the Fermi level. On the other hand, a GB between MoS<sub>2</sub> flakes with the same orientation shows a perfectly-stitched structure without any defects in scanned areas in STM images. We also found that both the conduction band minimum (CBM) and the valence band maximum (VBM) shift to the higher energy side at the GB even with a perfectly-stitched structure. This means that the GB state does not arise from defects but from strain at the GB, and strain formed at the growth process cannot be released even with the low friction coefficient between MoS<sub>2</sub> and graphite.

## 2. EXPERIMENTAL METHODS

We grew monolayer MoS<sub>2</sub> on hBN and graphite (Kish graphite, type C, Covalent Materials) flakes exfoliated on quartz substrates with a multi-furnace CVD apparatus. We prepared hBN and graphite flakes by the mechanical exfoliation method with adhesive tape (Scotch tape, 3M). As precursors for growth of MoS<sub>2</sub>, we used molybdenum trioxide (Sigma-Aldrich, 99.5% purity) and sulfur powder (Sigma-Aldrich, 99.98% purity). Furnace temperatures at the locations where molybdenum trioxide and elemental sulfur were placed were set to 1029 K and 473 K, respectively, and the growth of MoS<sub>2</sub> was carried out at 1373 K for 20 min under Ar flow with a flow rate of 200 sccm. We confirmed the monolayer structure by atomic force microscopy (AFM, Dimension 3100SPM, Nanoscope IV, Veeco) operated at a scanning rate of 1 Hz. We measured Raman spectra by a microspectroscopy system with a confocal microscope (Jobin Yvon HR-800, Horiba) with an excitation laser wavelength of 488 nm. For PL imaging, an LED light source (Mightex GCS-6500-15) was used, and PL intensity ( $\lambda > 600$  nm) was imaged with CCD (Princeton Instruments PIXIS-1024BR-eXelon).

We formed electrical contacts to samples for STM/STS measurements by

deposition of gold through a shadow mask or patterning conductive silver paste. After making the electrical contact, samples were introduced to an ultrahigh vacuum (UHV) environment and degassed at 473 K. The STM/STS measurements were conducted using a scanning tunneling microscope (Omicron LT–STM) in constant current mode operated at 90 K with an electrochemically etched W tip coated with PtIr (UNISOKU Co., Ltd.). A numerical derivative was used to acquire  $dI/dV$  curves, and WSxM software was used to process the STM images.<sup>[34]</sup>

### 3. RESULTS AND DISCUSSION

The crystal orientations of  $\text{MoS}_2$  grown on hBN and graphite are limited to two orientations due to the van der Waals interactions between  $\text{MoS}_2$  and hBN.

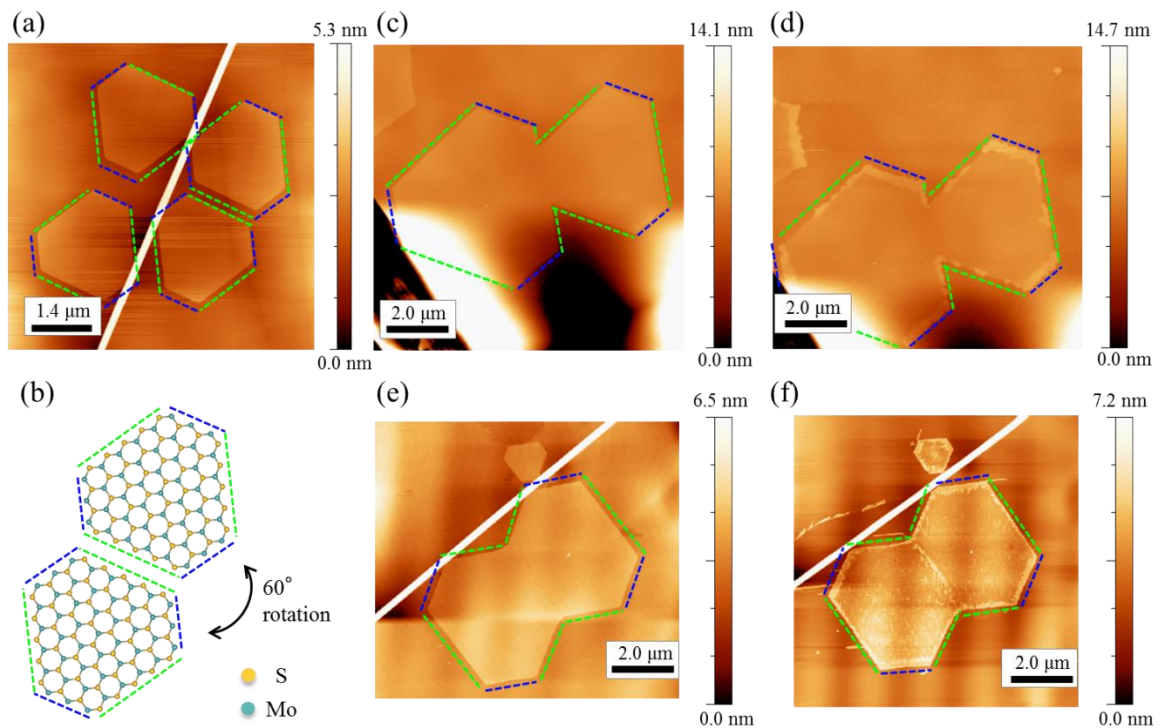


Figure 1. (a) An AFM image of monolayer  $\text{MoS}_2$  grown on h-BN. Long and short edges of  $\text{MoS}_2$  flakes are marked by green and blue dotted line, respectively. (b) Structural model of the grown  $\text{MoS}_2$  with relative angle of  $60^\circ$  degree. (c), (d) An AFM image of  $\text{MoS}_2$  before and after the oxidation. The relative angle between the two grains in this case is  $0^\circ$ . (e), (f) An AFM image of  $\text{MoS}_2$  before and after the oxidation. The relative angle between the two grains in this case is  $60^\circ$ . White linear contrasts in Figure 1(a), (c), and (f) are wrinkles in hBN flakes.

Figure 1(a) shows an AFM image of monolayer  $\text{MoS}_2$  crystals grown on a hBN flake. As clearly seen, all crystals possess a hexagonal shape with long and short

facets, and their orientations are limited to only two different ones, where  $60^\circ$  rotation of one orientation matches the other orientation. The observed long and short facets in the crystals correspond to chalcogen and metal zigzag edges; the relationship between crystal shape and crystallographic orientation was investigated with transmission electron microscopy and electron diffraction. Figure 1(b) shows structural models of hexagonal  $\text{MoS}_2$  flakes with the two different orientations. The limited orientations of  $\text{MoS}_2$  flakes are also observed in  $\text{MoS}_2$  flakes grown on graphite substrates. This clearly demonstrates that the orientation-dependent potential arising from crystalline substrates is crucial to limiting the crystal orientation of grown  $\text{MoS}_2$ .

Because the crystal orientation of  $\text{MoS}_2$  on hBN is limited, the resulting structure of the GBs should also be limited: GBs between grains with the same orientation (GB- $0^\circ$ ) and grains with  $60^\circ$  mutual orientation (GB- $60^\circ$ ). To investigate if defects exist at such GBs, we investigated the reactivity for an oxidation reaction.  $\text{MoS}_2$  flakes with GBs were heated at 573 K under a flow of dry air. It has been shown that defects are sensitive to oxidation and reactions under the conditions above lead to the formation of oxides. Because oxidation from  $\text{MoS}_2$  to the corresponding oxides heightens the pristine structure, position-sensitive detection of oxidation of  $\text{MoS}_2$  can easily be done through AFM height images. Figures 1(c) and (e) ((d) and (f)) are AFM images of pristine (oxidized)  $\text{MoS}_2$  flakes that have GB- $0^\circ$  and GB- $60^\circ$ , respectively. As clearly seen in Figs. 1(d) and (f), oxidation at Mo zigzag edges (shorter edges) is faster than that at S zigzag edges (longer edges).<sup>[35,36]</sup> We also found that GB- $60^\circ$  is oxidized as edges are oxidized, whereas GB- $0^\circ$  essentially retains its pristine structure. This means that GB- $0^\circ$  does not have defects that are sensitive to oxidation reactions, indicating that, unlike GB- $60^\circ$ , GB- $0^\circ$  has a well-stitched structure.

To investigate the structure and local electronic structure of GBs, we performed STM/STS measurements around the GBs. Figure 2(a) is a STM image of  $\text{MoS}_2$  grown on graphite, where positions of GB- $0^\circ$  are highlighted by arrows. As can be seen, the GB- $0^\circ$  image is slightly darker than its peripheral place, which indicates that GB- $0^\circ$  has different local density of states from its peripheral place. For detailed investigations of structure and electronic structure, atomic-resolution STM observation of the GB- $0^\circ$  was carried out. Figure 2(b) is a STM image of the GB- $0^\circ$  at high magnification, showing the triangular array of sulfur atoms as bright spots. GB- $0^\circ$  is imaged as slightly darker than its peripheral place at the middle of the STM topographic image, and we observed no defects at the GB- $0^\circ$ ; neither vacancies nor insertion of atomic rows are seen (Fig. 2(c) shows a

corresponding structure model). The well-stitched structure of GB-0° revealed by STM observation is consistent with its observed low reactivity toward oxidation reactions. It should be noted that a translational mismatch should exist at the boundary even with orientation matching between two grains. This result, however, clearly demonstrates that GB-0° has a perfectly stitched structure without any defects, indicating that the translational mismatch can be relaxed through sliding on the graphite plane. The ultraflat surfaces of graphite and MoS<sub>2</sub> may lead to ultralow friction between them, which should facilitate the sliding.<sup>[37-39]</sup>

As demonstrated by darker contrasts in the STM image, even though GB-0° has a well-stitched structure, the local electronic structure at GB-0° is different from that of its peripheral places. To see the differences in the electronic structures, we

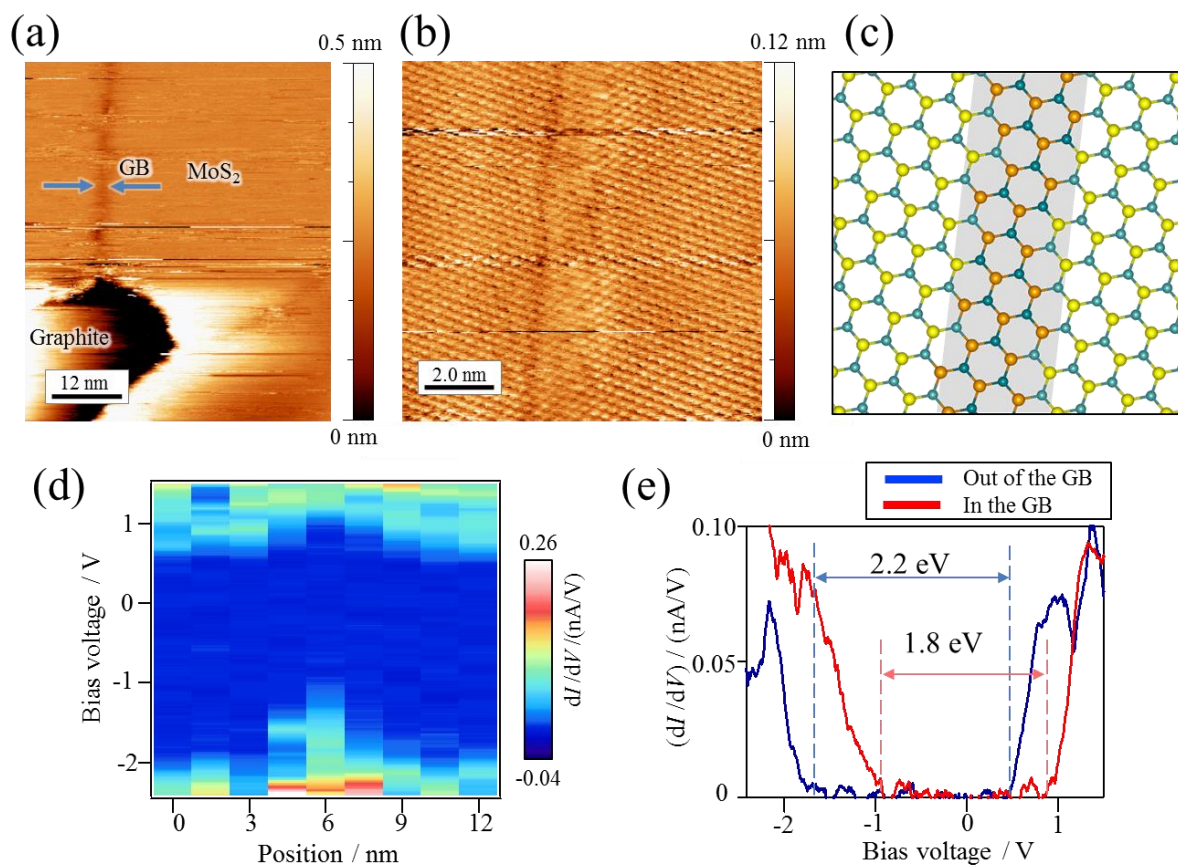


Figure 2. (a) An STM image of MoS<sub>2</sub> grown on graphite. The blue arrows indicate the position of GB. (b) A magnified STM image around the GB-0°. The GB-0° can be imaged as a dark linear contrast. (c) The corresponding structure model of the GB-0°, where two different grains are smoothly stitched to form a crystalline structure without defects. (d) dI/dV mapping across the GB-0°. (e) STS spectra measured at a place out of the GB and on the GB.

carried out STS and dI/dV mapping to visualize the local density of states. Figure 2(d) shows a dI/dV map across the GB-0°, which is located at a lateral position of

around 6 nm in Fig. 2(d). As clearly seen in the figure, both CBM and VBM show upward shifts at the GB-0°. Figure 2(e) is a STS spectrum at GB-0°, showing that the upward shift at VBM (0.8 eV) is larger than that at CBM (0.4 eV). This results in a reduction of the bandgap at the GB-0° from 2.2 eV to 1.8 eV; the observed bandgap of pristine monolayer MoS<sub>2</sub> (2.2 eV) is consistent with the value reported previously: 2.15–2.4 eV.<sup>[40-42]</sup> Because GB-0° has a perfectly stitched structure, this upward shift cannot be explained by formation of defects-mediated midgap states and can probably be explained by the local strain at the GB-0°. As monolayer MoS<sub>2</sub> has a non-centrosymmetric structure, the local strain can induce charge accumulation at the GB-0°, leading to the observed upward shift of CBM and VBM. One important implication is that a small strain remains even at GB-0°, where the local electronic structure is strongly altered.

To investigate the degree of strain at GB-0°, we performed fast Fourier transform (FFT) analysis on the STM image shown in Figure 2(b). As shown in Figure S4, a FFT image at GB-0° shows spots with 6-fold symmetry, which is consistent with a triangular lattice of the sulfur array. The 6-fold symmetric pattern in the FFT image of GB-0° is almost identical to a FFT image at a corresponding peripheral place; line profiles along the green arrows in the FFT image at GB-0° and the peripheral place also coincide well. This means that the difference in lattice constants at the GB-0° and its peripheral place is less than the experimental resolution (2%). As discussed above, the observed difference in bandgap at GB-0° and peripheral places is 0.4 eV. Assuming that the difference in bandgap originates only from lattice strain, the strain is estimated to be ~3%, which is smaller than the experimental resolution.

In the case of GB-60°, structural defects exist and the local electronic structure is strongly modified. Figure 3(a) is a STM image of MoS<sub>2</sub> on graphite near the GB-60°. The vertical linear contrast at the middle of the image corresponds to an impurity attached at GB-60°, where strong binding sites for impurities should exist. Figure 3(b) is a magnified STM image of clean GB-60°, where the atomic structure can be seen. In previous studies of STM/STS measurements of GB-60°, the atomic structure of GB-60° was not clear due to the adsorbate on GB-60°. Based on close investigation of the STM image, we found that the angle between GB-60° and the zigzag edge of MoS<sub>2</sub> is about 20°. Figure 3(d) shows the STS spectral mapping along the blue line in Figure 3(b). As clearly seen in Fig. 3(d), the electronic structure is significantly modulated at GB-60°, where both CBM and VBM upshift to reduce the bandgap from 2.3 eV to 1.9 eV. To investigate the spatial distribution of the boundary state at GB-60°, we performed dI/dV

mapping at three different bias voltages of 0.83, -0.78, and -1.54 V. Figures 3(e), (f), and (g) show the observed  $dI/dV$  mappings at bias voltages of 0.83, -0.78, and -1.54 V, respectively. As clearly seen, the boundary state strongly localizes at GB-60°. In addition, the boundary state corresponding to a bias voltage of -0.78 V shows a dotted distribution rather than a linear uniform distribution, and this means that the boundary state originates from a specific defect site existing at the GB-60°. Considering the previous ab initio calculations, the observed boundary state probably arises from the 8-4-4 membered ring structure.

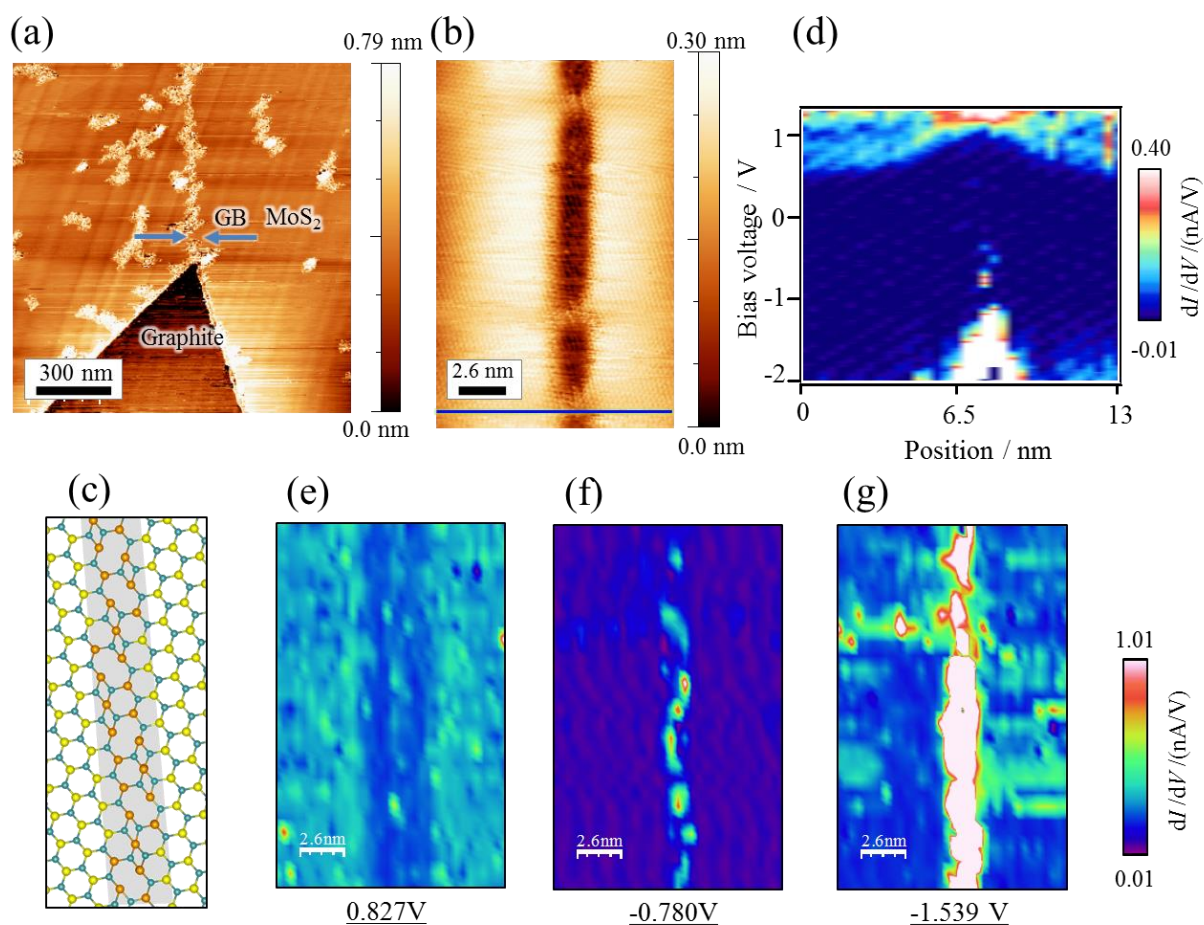


Figure 3. (a) An STM image of MoS<sub>2</sub> grown on graphite with a grain boundary of 60°. (b) A magnified STM image around the GB-60°. (c) The corresponding structure model of the GB-60°, where several defects formed. (d)  $dI/dV$  mapping across the GB-60°. (e), (f), and (g) STS spectral image of the GB-60° measured with different bias voltage of 0.827, -0.780, and -1.539 V, respectively.

#### 4. CONCLUSION

In this paper, electronic properties and defect densities in two types of GBs in

MoS<sub>2</sub> grown by the CVD process were investigated. The orientations of MoS<sub>2</sub> grown on hBN and graphite by the CVD process are limited to two directions and the misorientation angles of the two flakes are 0° and 60°. It is confirmed that two grains are stitched completely in the GB-0°, but have an upshift of band structure due to the local stress and charge accumulation. In the GB-60°, the structure of GB is clearly imaged by STM/STS without the disturbance of adsorbates on GB. The band structure in GB-60° upshifts and localized states appear. In the case of two grains of MoS<sub>2</sub> stitched at the same angle, the electronic structure of GB-0° is modified due to local stress and carrier accumulation. It will be a challenge to make a MoS<sub>2</sub> sheet without modulation of the electronic state or the structure.

## REFERENCES

- 1 P. Joensen, R. F. Frindt, and S. R. Morrison Single-Layer MoS<sub>2</sub> *Mater. Res. Bull.* **1986** 21 (4), 457-461.
- 2 B. Radisavljevic, A. Radenovic, J. Brivio, V. Giacometti, and A. Kis Single-layer MoS<sub>2</sub> transistors *Nat Nanotechnol* **2011** 6 (3), 147-150.
- 3 K. F. Mak, C. Lee, J. Hone, J. Shan, and T. F. Heinz Atomically Thin MoS<sub>2</sub>: A New Direct-Gap Semiconductor *Physical Review Letters* **2010** 105 (13), 136805.
- 4 G. B. Liu, D. Xiao, Y. G. Yao, X. D. Xu, and W. Yao Electronic structures and theoretical modelling of two-dimensional group-VIB transition metal dichalcogenides *Chem. Soc. Rev.* **2015** 44 (9), 2643-2663.
- 5 J. Pu and T. Takenobu Monolayer Transition Metal Dichalcogenides as Light Sources *Adv. Mater.* **2018** 30 (33), 1707627.
- 6 Q. H. Wang, K. Kalantar-Zadeh, A. Kis, J. N. Coleman, and M. S. Strano Electronics and optoelectronics of two-dimensional transition metal dichalcogenides *Nat Nanotechnol* **2012** 7 (11), 699-712.
- 7 D. Jariwala, V. K. Sangwan, L. J. Lauhon, T. J. Marks, and M. C. Hersam Emerging Device Applications for Semiconducting Two-Dimensional Transition Metal Dichalcogenides *Acs Nano* **2014** 8 (2), 1102-1120.
- 8 G. H. Lee, Y. J. Yu, X. Cui, N. Petrone, C. H. Lee, M. S. Choi, D. Y. Lee, C. Lee, W. J. Yoo, K. Watanabe, T. Taniguchi, C. Nuckolls, P. Kim, and J. Hone Flexible and Transparent MoS<sub>2</sub> Field-Effect Transistors on

- Hexagonal Boron Nitride-Graphene Heterostructures *Acs Nano* **2013** 7 (9), 7931-7936.
- 9 J. Pu, Y. Yomogida, K. K. Liu, L. J. Li, Y. Iwasa, and T. Takenobu Highly Flexible MoS<sub>2</sub> Thin-Film Transistors with Ion Gel Dielectrics *Nano Letters* **2012** 12 (8), 4013-4017.
- 10 D. Xiao, G. B. Liu, W. X. Feng, X. D. Xu, and W. Yao Coupled Spin and Valley Physics in Monolayers of MoS<sub>2</sub> and Other Group-VI Dichalcogenides *Physical Review Letters* **2012** 108 (19), 196802.
- 11 J. R. Schaibley, H. Y. Yu, G. Clark, P. Rivera, J. S. Ross, K. L. Seyler, W. Yao, and X. D. Xu Valleytronics in 2D materials *Nat Rev Mater* **2016** 1 (11), 16055.
- 12 R. Kitaura, Y. Miyata, R. Xiang, J. Hone, J. Kong, R. S. Ruoff, and S. Maruyama Chemical Vapor Deposition Growth of Graphene and Related Materials *Journal of the Physical Society of Japan* **2015** 84 (12), 121013.
- 13 Y. M. Shi, H. N. Li, and L. J. Li Recent advances in controlled synthesis of two-dimensional transition metal dichalcogenides via vapour deposition techniques *Chem. Soc. Rev.* **2015** 44 (9), 2744-2756.
- 14 K. S. Novoselov, D. Jiang, F. Schedin, T. J. Booth, V. V. Khotkevich, S. V. Morozov, and A. K. Geim Two-dimensional atomic crystals *P Natl Acad Sci USA* **2005** 102 (30), 10451-10453.
- 15 Y. H. Lee, X. Q. Zhang, W. J. Zhang, M. T. Chang, C. T. Lin, K. D. Chang, Y. C. Yu, J. T. W. Wang, C. S. Chang, L. J. Li, and T. W. Lin Synthesis of Large-Area MoS<sub>2</sub> Atomic Layers with Chemical Vapor Deposition *Adv. Mater.* **2012** 24 (17), 2320-2325.
- 16 A. Reina, X. T. Jia, J. Ho, D. Nezich, H. B. Son, V. Bulovic, M. S. Dresselhaus, and J. Kong Large Area, Few-Layer Graphene Films on Arbitrary Substrates by Chemical Vapor Deposition *Nano Letters* **2009** 9 (1), 30-35.
- 17 S. Sinha, Y. Takabayashi, H. Shinohara, and R. Kitaura Simple fabrication of air-stable black phosphorus heterostructures with large-area hBN sheets grown by chemical vapor deposition method *2d Mater* **2016** 3 (3), 035010.
- 18 M. Okada, Y. Miyauchi, K. Matsuda, T. Taniguchi, K. Watanabe, H. Shinohara, and R. Kitaura Observation of biexcitonic emission at extremely low power density in tungsten disulfide atomic layers grown on hexagonal boron nitride *Sci Rep-Uk* **2017** 7, 322.
- 19 Y. Kobayashi, S. Sasaki, S. Mori, H. Hibino, Z. Liu, K. Watanabe, T.

- Taniguchi, K. Suenaga, Y. Maniwa, and Y. Miyata Growth and Optical Properties of High-Quality Monolayer WS<sub>2</sub> on Graphite *Acs Nano* **2015** 9 (4), 4056-4063.
- 20 M. Okada, T. Sawazaki, K. Watanabe, T. Taniguch, H. Hibino, H. Shinohara, and R. Kitaura Direct Chemical Vapor Deposition Growth of WS<sub>2</sub> Atomic Layers on Hexagonal Boron Nitride *Acs Nano* **2014** 8 (8), 8273-8277.
- 21 Y. J. Zhan, Z. Liu, S. Najmaei, P. M. Ajayan, and J. Lou Large-Area Vapor-Phase Growth and Characterization of MoS<sub>2</sub> Atomic Layers on a SiO<sub>2</sub> Substrate *Small* **2012** 8 (7), 966-971.
- 22 S. M. Eichfeld, L. Hossain, Y. C. Lin, A. F. Piasecki, B. Kupp, A. G. Birdwell, R. A. Burke, N. Lu, X. Peng, J. Li, A. Azcatl, S. McDonnell, R. M. Wallace, M. J. Kim, T. S. Mayer, J. M. Redwing, and J. A. Robinson Highly Scalable, Atomically Thin WSe<sub>2</sub> Grown via Metal-Organic Chemical Vapor Deposition *Acs Nano* **2015** 9 (2), 2080-2087.
- 23 H. Kim, D. Ovchinnikov, D. Deiana, D. Unuchek, and A. Kis Suppressing Nucleation in Metal-Organic Chemical Vapor Deposition of MoS<sub>2</sub> Monolayers by Alkali Metal Halides *Nano Letters* **2017** 17 (8), 5056-5063.
- 24 K. Kang, S. E. Xie, L. J. Huang, Y. M. Han, P. Y. Huang, K. F. Mak, C. J. Kim, D. Muller, and J. Park High-mobility three-atom-thick semiconducting films with wafer-scale homogeneity *Nature* **2015** 520 (7549), 656-660.
- 25 A. M. van der Zande, P. Y. Huang, D. A. Chenet, T. C. Berkelbach, Y. M. You, G. H. Lee, T. F. Heinz, D. R. Reichman, D. A. Muller, and J. C. Hone Grains and grain boundaries in highly crystalline monolayer molybdenum disulphide *Nature Materials* **2013** 12 (6), 554-561.
- 26 H. G. Ji, Y. C. Lin, K. Nagashio, M. Maruyama, P. Solis-Fernandez, A. S. Aji, V. Panchal, S. Okada, K. Suenaga, and H. Ago Hydrogen-Assisted Epitaxial Growth of Monolayer Tungsten Disulfide and Seamless Grain Stitching *Chem. Mater.* **2018** 30 (2), 403-411.
- 27 K. Elibol, T. Susi, M. O'Brien, B. C. Bayer, T. J. Pennycook, N. McEvoy, G. S. Duesberg, J. C. Meyer, and J. Kotakoski Grain boundary-mediated nanopores in molybdenum disulfide grown by chemical vapor deposition *Nanoscale* **2017** 9 (4), 1591-1598.
- 28 L. Karvonen, A. Saynatjoki, M. J. Huttunen, A. Autere, B.

- Amirsolaimani, S. Li, R. A. Norwood, N. Peyghambarian, H. Lipsanen, G. Eda, K. Kieu, and Z. P. Sun Rapid visualization of grain boundaries in monolayer MoS<sub>2</sub> by multiphoton microscopy *Nat Commun* **2017** 8, 15714.
- 29 H. Yu, Z. Z. Yang, L. J. Du, J. Zhang, J. N. Shi, W. Chen, P. Chen, M. Z. Liao, J. Zhao, J. L. Meng, G. L. Wang, J. Q. Zhu, R. Yang, D. X. Shi, L. Gu, and G. Y. Zhang Precisely Aligned Monolayer MoS<sub>2</sub> Epitaxially Grown on h-BN basal Plane *Small* **2017** 13 (7), 1603005.
- 30 S. Najmaei, Z. Liu, W. Zhou, X. L. Zou, G. Shi, S. D. Lei, B. I. Yakobson, J. C. Idrobo, P. M. Ajayan, and J. Lou Vapour phase growth and grain boundary structure of molybdenum disulphide atomic layers *Nature Materials* **2013** 12 (8), 754-759.
- 31 W. Zhou, X. L. Zou, S. Najmaei, Z. Liu, Y. M. Shi, J. Kong, J. Lou, P. M. Ajayan, B. I. Yakobson, and J. C. Idrobo Intrinsic Structural Defects in Monolayer Molybdenum Disulfide *Nano Letters* **2013** 13 (6), 2615-2622.
- 32 T. Hotta, T. Tokuda, S. Zhao, K. Watanabe, T. Taniguchi, H. Shinohara, and R. Kitaura Molecular beam epitaxy growth of monolayer niobium diselenide flakes *Applied Physics Letters* **2016** 109 (13), 133101.
- 33 H. Ago, H. Endo, P. Solis-Fernandez, R. Takizawa, Y. Ohta, Y. Fujita, K. Yamamoto, and M. Tsuji Controlled van der Waals Epitaxy of Mono layer MoS<sub>2</sub> Triangular Domains on Graphene *Acs Appl Mater Inter* **2015** 7 (9), 5265-5273.
- 34 I. Horcas, R. Fernandez, J. M. Gomez-Rodriguez, J. Colchero, J. Gomez-Herrero, and A. M. Baro WSXM: A software for scanning probe microscopy and a tool for nanotechnology *Review of Scientific Instruments* **2007** 78 (1), 013705.
- 35 M. Yamamoto, S. Dutta, S. Aikawa, S. Nakaharai, K. Wakabayashi, M. S. Fuhrer, K. Ueno, and K. Tsukagoshi Self-Limiting Layer-by-Layer Oxidation of Atomically Thin WSe<sub>2</sub> *Nano Letters* **2015** 15 (3), 2067-2073.
- 36 J. V. Lauritsen, J. Kibsgaard, S. Helveg, H. Topsoe, B. S. Clausen, E. Laegsgaard, and F. Besenbacher Size-dependent structure of MoS<sub>2</sub> nanocrystals *Nat Nanotechnol* **2007** 2 (1), 53-58.
- 37 Y. Kobayashi, T. Taniguchi, K. Watanabe, Y. Maniwa, and Y. Miyata Slidable atomic layers in van der Waals heterostructures *Appl Phys Express* **2017** 10 (4), 045201.

- 38 D. Mandelli, I. Leven, O. Hod, and M. Urbakh Sliding friction of graphene/hexagonal boron nitride heterojunctions: a route to robust superlubricity *Sci Rep-Uk* **2017** 7, 10851.
- 39 L. F. Wang, X. Zhou, T. B. Ma, D. M. Liu, L. Gao, X. Li, J. Zhang, Y. Z. Hu, H. Wang, Y. D. Dai, and J. B. Luo Superlubricity of a graphene/MoS<sub>2</sub> heterostructure: a combined experimental and DFT study *Nanoscale* **2017** 9 (30), 10846-10853.
- 40 H. Li, A. W. Contryman, X. F. Qian, S. M. Ardakani, Y. J. Gong, X. L. Wang, J. M. Weisse, C. H. Lee, J. H. Zhao, P. M. Ajayan, J. Li, H. C. Manoharan, and X. L. Zheng Optoelectronic crystal of artificial atoms in strain-textured molybdenum disulphide *Nat Commun* **2015** 6, 7381.
- 41 X. L. Liu, I. Balla, H. Bergeron, and M. C. Hersam Point Defects and Grain Boundaries in Rotationally Commensurate MoS<sub>2</sub> on Epitaxial Graphene *Journal of Physical Chemistry C* **2016** 120 (37), 20798-20805.
- 42 Y. L. Huang, Y. F. Chen, W. J. Zhang, S. Y. Quek, C. H. Chen, L. J. Li, W. T. Hsu, W. H. Chang, Y. J. Zheng, W. Chen, and A. T. S. Wee Bandgap tunability at single-layer molybdenum disulphide grain boundaries *Nat Commun* **2015** 6, 6298.